Communication

Mainlobe Deceptive Jammer Suppression Based on Quadratic Phase Coding in FDA-MIMO Radar

Yiqun Zhang, Guisheng Liao, Jingwei Xu * and **Lan Lan**

National Key Laboratory of Radar Signal Processing, Xidian University, Xi'an 710071, China
* Correspondence: jwxu@xidian.edu.cn; Tel.: +86-181-9203-9179

Abstract: In this paper, the problem of mainlobe deceptive jammer suppression is solved with the frequency diversity array-multiple-input multiple-output (FDA-MIMO) radar system. At the modeling stage, based on the FDA-MIMO radar, a quadratic phase code (QPC) is applied along the slow time dimension in the transmit array. In the receiver, after decoding and principal range compensation, the true and false targets that are generated in an identical angle, can be discriminated in the joint transmit-receive-Doppler frequency domain. Particularly, the false targets are equivalently moved from the mainlobe to the sidelobes in the transmit spatial frequency domain. Then, by performing the data-dependent transmit-receive-Doppler three-dimensional beamforming, the false targets are suppressed owing to Doppler and range mismatches. Moreover, by moving the jammers to nulls in the Doppler frequency domain, the capability in terms of the maximum number of suppressible jammers can be strengthened with an appropriate coding coefficient and frequency increment. Numerical results can certify the suppression capability of the QPC-FDA-MIMO radar.

Keywords: mainlobe deceptive jammer suppression; quadratic phase code; three-dimensional beamforming; FDA-MIMO radar

1. Introduction

Radar systems have been widely used in military and civil applications owing to their advantages of detecting targets in all-time and all-whether [1,2]. However, in the complex electromagnetic environment, the jamming signals pose a severe threat to radar systems [3,4]. Among distinct types of jammers, deceptive jammers are generated by intercepting the radar's waveform and re-transmitting it to fool the victim radars, making it tough to discriminate between false targets and true ones [5]. Particularly, after some appropriate modulations of the digital radio frequency memory (DRFM), the deception is strengthened, and the false targets are produced with parameters such as angle, waveform, and frequency the same as that of the true target [6,7]. The jammers which are situated at the sidelobes of the radar antenna beam can be effectively suppressed via spatial processing methods, such as generalized sidelobe canceller (GSC), ultra-low sidelobe antennas, and space-time adaptive processing (STAP) [8,9]. However, the suppression of mainlobe deceptive jammers is more challenging due to limited degrees-of-freedom (DOFs) to distinguish the true one from the false targets in the angle domain.

At present, methods to suppress mainlobe jammers have been explored by exploiting the discrepancies between the false targets and the true target in various domains, such as the time domain [10], frequency domain [11–13], spatial domain [14], and polarization domain [15]. Particularly, pulse frequency agility was utilized in [16] by adopting distinct frequencies among the transmit pulses. However, the coherence among pulses cannot be ensured. Considering the suppression methods in the spatial domain, the methods based on compressed sensing were utilized to reconstruct the echo signal for intermittent sampling jammer [17]. In addition, the projection matrix/blocking matrix was utilized [18,19].

Nevertheless, the projection matrix/blocking matrix is difficult to construct and the methods are sensitive to errors. Moreover, the signal can be separated from the source signal based on the blind source separation [20–22]. However, the jammers and target must be independent or less correlated, and additional prior knowledge is required to estimate the number of sources. In [23–25], the polarization filter was designed to suppress the jammers. However, some considerable limitations in practice exist when using the aforementioned methods for suppressing the mainlobe deceptive jammers with the characteristics of high density and high fidelity. Thus, it is worth investigating suppression approaches based on novel radar frameworks.

In the decade, the frequency diversity array-multiple-input multiple-output (FDA-MIMO) radar has attracted extensive attention. Unlike the phased array radar, a frequency increment is adopted between all the adjacent elements in the transmit array, and the range-angle-dependent transmit beampattern is generated [26–28]. Hence, extra DOFs in the range domain are obtained, and the flexibility in signal processing is improved [29]. To this end, a large number of studies are focused on jammer suppression by utilizing data-dependent and data-independent beamforming methods in the FDA-MIMO radar, where the false targets are suppressed by means of nulling in the joint transmit-receive spatial domain [30–34]. Moreover, the PBN-BF method was utilized to improve the robustness of jammer suppression by broadening the nulls [35]. In addition, similar to FDA-MIMO radar, the suppression of mainlobe deceptive jammers with the Element-Pulse-Coding (EPC)-MIMO radar was investigated [35–37]. Moreover, a new technology based on polarization was developed in [38] by jointly utilizing the information including the angle, range, as well as polarization to suppress the jammers. Additionally, a low-rank-low-rank-sparse method was proposed to recover the signal of the target and suppresses the blocking jamming [39]. In [40], an optimization model was established by considering the frequency increments regulation based on non-uniformly spaced FDA radar. However, the maximum number of jammers with such a method equals that of the transmit elements. In other words, the performance of jammer suppression is limited to the system DOFs.

In this paper, to address the issue of mainlobe jammer suppression, a novel coding scheme in FDA-MIMO is suggested. During the modeling phase, a quadratic phase code (QPC) is introduced in the slow time pulses. In this regard, extra DOFs in both range and Doppler domains can be obtained. In the receiver, after decoding and principal range compensation, the true and false targets that locate a couple of pulses behind the true target are discriminated in the joint transmit-receive and Doppler frequency domain. In particular, these false targets are equivalently moved to the sidelobes of the equivalent transmit beam pattern. Furthermore, the data-dependent transmit-receive-Doppler three-dimensional beamforming is developed to suppress the false targets by means of nulling in the transmit-receive-Doppler domain due to range and Doppler mismatches. At the analysis stage, the designs of the coding coefficient and frequency increment are investigated to increase the number of suppressible false targets, where the jammers are moved to the nulls in the beampattern of the Doppler frequency domain. Furthermore, to illustrate the effectiveness of the mentioned suppression method, the simulation results are provided.

In this paper, the structure is given as follows. The QPC-FDA-MIMO radar system's signal model is provided in Section 2. The principle of main lobe deceptive jammer suppression with the QPC-FDA-MIMO radar is investigated in Section 3. To demonstrate the performance of the developed approaches, the numerical simulations are presented in Section 4. In Section 5, conclusions are drawn.

2. Signal Model of FDA-MIMO Radar

2.1. Transmit Signal Model

A collocated MIMO radar is considered in a uniform linear array with N transmit and M receive elements, where the first element is taken as the reference. A small frequency

increment Δf is introduced across the array elements, and the carrier frequency of the *m*-th element is assigned as

$$f_m = f_0 + (m-1)\Delta f, \ m = 1,2,\cdots,M \tag{1}$$

where f_0 indicates the reference carrier frequency.

Different from the conventional FDA-MIMO radar, the QPC factor of the *k*-th pulse is designed as $\varphi_{\mathrm{mod}}(k) = \exp\{j\pi\gamma k^2\}$ with γ the coding coefficient. Hence, the signal which is transmitted by the *m*-th antenna element is:

$$s_{m,k}(t) = \sqrt{\frac{E}{M}}\mathrm{rect}\left(\frac{t}{T_p}\right)\Phi_m(t)\exp\{j2\pi f_m t\}\varphi_{\mathrm{mod}}(k) \tag{2}$$

where T_p denotes the radar pulse duration, E is the total energy, $\mathrm{rect}\left(\frac{t}{T_p}\right) = \begin{cases} 1, 0 < t < T_P \\ 0, \ else \end{cases}$,

$\Phi_m(t)$ indicates the orthogonal waveform transmitted by the *m*-th element with the complex envelope

$$\Phi_m(t) = \frac{1}{\sqrt{\tau_b}}\sum_{l=1}^{L}g_m(l)rect\left(\frac{t-(l-1)\tau_b}{\tau_b}\right), \ l = 1,\ldots,L \tag{3}$$

where $\tau_b = \frac{T_p}{L}$ is the length of the subpulse, L is the number of the subpulses, $g_m(l) = e^{jz_m(l)}, z_m(l) \in [0,2\pi]$.

2.2. Receive Signal Model

Assume that there is a point-like target in the far-field at angle θ and range R_s, whose delayed pulse number is q_s. Considering *K* pulses, the coding phase related to the *k*-th ($k = 1,\cdots,K$) pulse can be expressed as:

$$\varphi_{\mathrm{mod,s}}(k) = e^{j\pi\gamma(k-q_\mathrm{s})^2} \tag{4}$$

The signal that is received by the *n*-th ($n = 1,\cdots,N$) element is expressed as:

$$x_{n,k}(t-\tau_{m,n}) \approx \xi\mathrm{rect}\left(\frac{t-\tau_0}{T_p}\right)\sum_{m=1}^{M}\Phi_{m,k}(t-\tau_0)e^{j2\pi\Delta f(m-1)(t-\tau_{m,n}+(k-1)T_r)}e^{j2\pi f_0(t-\tau_{m,n}+(k-1)T_r)}e^{j2\pi f_d(k-1)T_r}\varphi_{\mathrm{mod,s}}(k) \tag{5}$$

where the approximation holds for the assumption of a narrow band, ξ represents the complex coefficient of the point target. $\tau_{m,n} = \tau_0 - \frac{(m-1)d\sin(\theta)}{c} - \frac{(n-1)d\sin(\theta)}{c}$ represents the round-trip propagation time delay, $\tau_0 = \frac{2R_\mathrm{s}}{c}$ represents the common time delay, *d* donates the inter-element spacing. $f_\mathrm{d} = \frac{2v_\mathrm{s}}{\lambda_0}$ is the Doppler frequency of the target with v_s and λ_0, the target speed and wavelength, respectively.

Firstly, the received signal is mixed with $e^{-j2\pi f_0 t}$. Then, as is shown in Figure 1, a group of filters is utilized on each receive channel. What is more, take the *l*-th ($l = 1,2,\ldots M$) filter as an example, and the received signal is firstly multiplied with $e^{-j2\pi\Delta f(l-1)t}$. Subsequently, the transmitted waveforms are separated via matched filtering, where the *l*-th matched filter is denoted as $h_l(t) = x_l^*(-t)$, and the resulting signal is written as

$$x_{n,k}(t) \approx \xi e^{-j2\pi f_0\tau_{m,n}}\mathrm{rect}\left(\frac{t-\tau_0}{T_p}\right)e^{-j2\pi\Delta f(m-1)\tau_{m,n}+j2\pi f_d(k-1)T_r}\varphi_{\mathrm{mod,s}}(k)\sin\mathrm{c}(t-\tau_0) \tag{6}$$
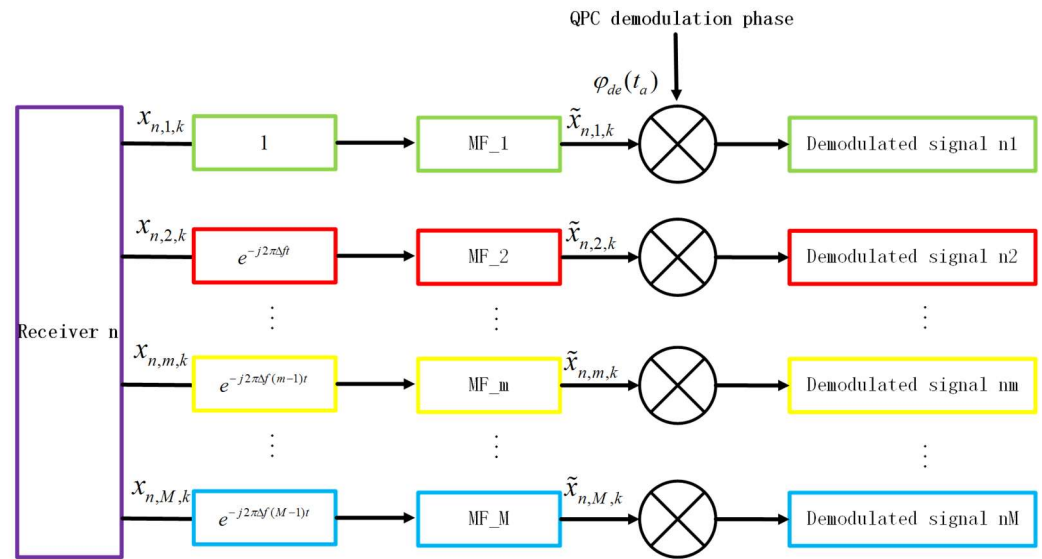
Figure 1. Procedures of receive processing.

Subsequently, the QPC demodulation is performed along the slow time, and the demodulation phase of each receive array element in the k-th pulse is defined as

$$\varphi_{\mathrm{de}}(k) = e^{-j\pi\gamma k^2} \tag{7}$$

After QPC demodulation, the residual phase is expressed as

$$\varphi_{\mathrm{res}}(k) = \varphi_{\mathrm{mod,s}}(k)\varphi_{\mathrm{de}}(k) = e^{-j2\pi\Delta f_{\mathrm{s}}k}e^{j\pi q_{\mathrm{s}}^2\gamma} \tag{8}$$

where the first exponential term is linearly dependent on k, Δf_{s} indicates the additional normalized Doppler shift, which is expressed as

$$\Delta f_{\mathrm{s}} = q_{\mathrm{s}}\gamma \tag{9}$$

By stacking the received signals corresponding to N receive elements with K pulses, the received signal is organized as an $MN \times K$-dimensional vector, i.e.,

$$\boldsymbol{Y}_{\mathrm{s}} = \alpha\{\boldsymbol{r} \odot [\boldsymbol{b}(\theta) \otimes \boldsymbol{a}(R_{\mathrm{s}},\theta)]\}\boldsymbol{h}^{\mathrm{T}}(f_{\mathrm{D}} - \Delta f_{\mathrm{s}}) \tag{10}$$

where $\boldsymbol{r} = \boldsymbol{1}_N \otimes \widetilde{\boldsymbol{r}} \in C^{MN \times 1}$ with $\widetilde{\boldsymbol{r}} = [\widetilde{r}_1, \widetilde{r}_2, \dots, \widetilde{r}_M]^{\mathrm{T}} \in C^{N \times 1}$ is the output vector after matched filtering, and $f_{\mathrm{D}} = \frac{f_{\mathrm{d}}}{f_{\mathrm{PRF}}}$ is the targets' normalized Doppler frequency. $\boldsymbol{h}(f_{\mathrm{D}} - \Delta f_{\mathrm{s}}) \in C^{K \times 1}$, $\boldsymbol{b}(\theta) \in C^{N \times 1}$ and $\boldsymbol{a}(R_{\mathrm{s}},\theta) \in C^{M \times 1}$, respectively, denote the Doppler vector, the receive steering vector, and the transmit steering vector, with the forms of

$$\boldsymbol{h}(f_{\mathrm{D}} - \Delta f_{\mathrm{s}}) = [1, e^{j2\pi(f_{\mathrm{D}} - \Delta f_{\mathrm{s}})}, \dots, e^{j2\pi(f_{\mathrm{D}} - \Delta f_{\mathrm{s}})(K-1)}]^{\mathrm{T}} \tag{11}$$

$$\boldsymbol{b}(\theta) = [1, e^{j2\pi\frac{d}{\lambda}\sin\theta}, \dots, e^{j2\pi\frac{d}{\lambda}\sin\theta(N-1)}]^{\mathrm{T}} \tag{12}$$

$$\boldsymbol{a}(R_{\mathrm{s}},\theta) = [1, e^{-j2\pi\Delta f\frac{R_{\mathrm{s}}}{c}}, \dots, e^{-j2\pi\Delta f\frac{R_{\mathrm{s}}}{c}(M-1)}]^{\mathrm{T}} \odot [1, e^{j2\pi\frac{d}{\lambda}\sin\theta}, \dots, e^{j2\pi\frac{d}{\lambda}\sin\theta(M-1)}]^{\mathrm{T}} \tag{13}$$

3. Principle of Mainlobe Deceptive Jammer Suppression in QPC-FDA-MIMO

3.1. Generation of False Targets

Consider a self-defense deception jammer equipped with a false target generator (FTG) situated at an identical angle to the true one, where the range deception is achieved with several pseudo-randomly distributed false targets after some appropriate modulation in DRFM. Actually, the false targets are located behind the true one either in the same received

pulse or at least one transmit pulse. In this paper, the latter case is concentrated on, namely, the false targets and the true target have distinct numbers of delayed pulses.

The generation of the false targets in the QPC-FDA-MIMO radar is shown in Figure 2, where the two false targets locate at least one slow time pulse behind the true one. However, in an identical receive pulse, the false targets can be either ahead of the target, that is, the false target 1, or behind the true one, that is, the false target 2. Moreover, QPC is implemented among pulses while it is identical for all transmit elements.
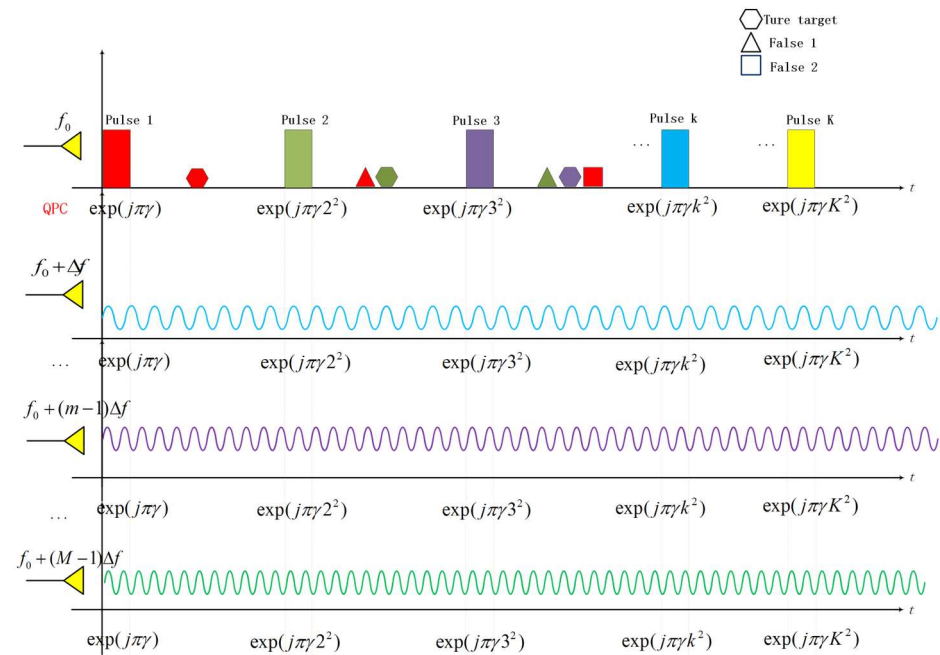

Figure 2. Illumination of true and false targets with QPC-FDA-MIMO.

Let us consider H false targets and a case study of the h-th ($h = 1, 2, \ldots, H$) false target, whose number of delayed pulses is q_{jh}, and its QPC code is the same as the $k - q_j$-th pulse as shown in Figure 2. Hence, the QPC code of the h-th false target is expressed as

$$\Phi_{\mathrm{mod,j}}(k) = e^{j\pi\gamma(k-q_{jh})^2} \tag{14}$$

Then, after QPC demodulation, the residual phase is

$$\Phi_{\mathrm{res,j}}(k) = e^{-j2\pi\Delta f_{jh}k} e^{j\pi q_{jh}^2\gamma} \tag{15}$$

where Δf_{jh} denotes the additional normalized Doppler frequencies of the false target, i.e.,

$$\Delta f_{jh} = q_{jh}\gamma \tag{16}$$

By collecting the received signals from all elements, the received jamming signal can be stacked into an $MN \times K$-dimensional vector, i.e.,

$$Y_j = \alpha\big\{r \odot [b(\theta) \otimes a(R_j, \theta)]\big\} h^{\mathrm{T}}(f_{\mathrm{D}} - \Delta f_{jh}) \tag{17}$$

where R_j denotes the equivalent location of the h-th false target after time modulation in the FTG, $h(f_{\mathrm{D}} - \Delta f_{jh}) \in C^{K \times 1}$ and $a(R_j, \theta) \in C^{M \times 1}$ denote the Doppler vector and the transmit steering vector of the h-th false target, respectively with the forms of

$$h(f_{\mathrm{D}} - \Delta f_{jh}) = [1, e^{j2\pi(f_{\mathrm{D}} - \Delta f_{jh})}, \ldots, e^{j2\pi(f_{\mathrm{D}} - \Delta f_{jh})(K-1)}]^{\mathrm{T}} \tag{18}$$

$$\boldsymbol{a}(R_{\mathrm{j}}, \theta) = \left[1, e^{-j2\pi\Delta f \frac{R_{\mathrm{j}}}{c}}, \ldots, e^{-j2\pi\Delta f \frac{R_{\mathrm{j}}}{c}(M-1)}\right]^{\mathrm{T}} \odot \left[1, e^{j2\pi \frac{d}{\lambda}\sin\theta}, \ldots, e^{j2\pi \frac{d}{\lambda}\sin\theta(M-1)}\right]^{\mathrm{T}} \quad (19)$$

It can be observed from (19) that after QPC demodulation, the false targets and the true target have distinct additional normalized Doppler shifts. Hence, the false targets and the true target are can be discriminated in the Doppler frequency domain.

Furthermore, the total received signal, considering H false targets, the true target and the noise component, is expressed as

$$\boldsymbol{Y} = \sum_{h=1}^{H} \boldsymbol{Y}_{\mathrm{jh}} + \boldsymbol{Y}_{\mathrm{s}} + \boldsymbol{N} \quad (20)$$

where $\boldsymbol{N} \sim \mathcal{CN}\left(0, \sigma^2 I_{MN}\right)$ denotes the white Gaussian noise with $\boldsymbol{R}_{\mathrm{n}} = \sigma^2 I_{MN}$ the covariance matrix, I_{MN} donates the $MN \times MN$-dimensional identity matrix, and σ^2 donates the noise power.

3.2. Mainlobe Deceptive Jammer Suppression

Based on the transmit and receive steering vectors in the QPC-FDA-MIMO radar, the transmit spatial frequencies of the true and the h-th false targets are:

$$f_{\mathrm{T,s}} = -\frac{2\Delta f R_{\mathrm{s}}}{c} + \frac{d_{\mathrm{T}}}{\lambda_0}\sin(\theta) \quad (21)$$

$$f_{\mathrm{T,j}} = -\frac{2\Delta f R_{\mathrm{j}}}{c} + \frac{d_{\mathrm{T}}}{\lambda_0}\sin(\theta) \quad (22)$$

where R_{s} and R_{j} are the actual ranges of the true and the h-th false target, which are represented as

$$R_{\mathrm{s}} = R_{\mathrm{u}}q_{\mathrm{s}} + r_{\mathrm{s}} \quad (23)$$

$$R_{\mathrm{j}} = R_{\mathrm{u}}q_{\mathrm{jh}} + r_{\mathrm{j}} \quad (24)$$

where $R_u = c/(2f_{\mathrm{PRF}})$ indicates the maximum unambiguous range with f_{PRF} the pulse repetition frequency. r_{s} and r_{j} indicate the principal ranges of the true target and the h-th false target, respectively.

Specifically, let us construct the compensating vector as [30]

$$\boldsymbol{y}_1 = \left[1, e^{j2\pi f_{c1}}, \cdots, e^{j2\pi f_{c1}(M-1)}\right]^{\mathrm{T}} \quad (25)$$

where $f_{c1} = \frac{2r_a\Delta f}{c}$ is the range compensating frequency, and r_a is the principal range obtained by the range bin size and the range bin number.

What is more, the receive-transmit joint compensation vector is constructed as

$$\boldsymbol{A} = \boldsymbol{1}_{N\times K} \otimes \boldsymbol{y}_1 \quad (26)$$

Then, the received data are compensated as

$$\widetilde{\boldsymbol{Y}} = \boldsymbol{A} \odot \boldsymbol{Y} \quad (27)$$

After the compensation range, bin-by range bin [34], the ranges of the true and the h-th false target can be, respectively, written as

$$\widetilde{R}_{\mathrm{s}} = R_{\mathrm{u}}q_{\mathrm{s}} \quad (28)$$

$$\widetilde{R}_{\mathrm{j}} = R_{\mathrm{u}}q_{\mathrm{jh}} \quad (29)$$

Accordingly, the transmit spatial frequencies of the true and the *h*-th false target are

$$\widetilde{f}_{T,s} = -\frac{2\Delta f R_u q_s}{c} + \frac{d_T}{\lambda_0}\sin(\theta) \tag{30}$$

$$\widetilde{f}_{T,j} = -\frac{2\Delta f R_u q_{jh}}{c} + \frac{d_T}{\lambda_0}\sin(\theta) \tag{31}$$

Hence, the targets relative to distinct range bins are concentrated in an identical receive pulse after range compensation [34]. In other words, the transmit spatial frequencies of the targets that are located in the same pulses (i.e., the range ambiguity region) are equal. As shown in Figure 3, after compensation, the false targets 1 and 2 are situated in the same position in the joint transmit-receive spatial frequency domain for the reason that they have identical delayed pulses. However, the false target 4 and the true target cannot be distinguished in the transmit-receive spatial domain because the number of delayed pulses is *M*. In order to discriminate the false target 4 and the true one, it is necessary to utilize the Doppler information.
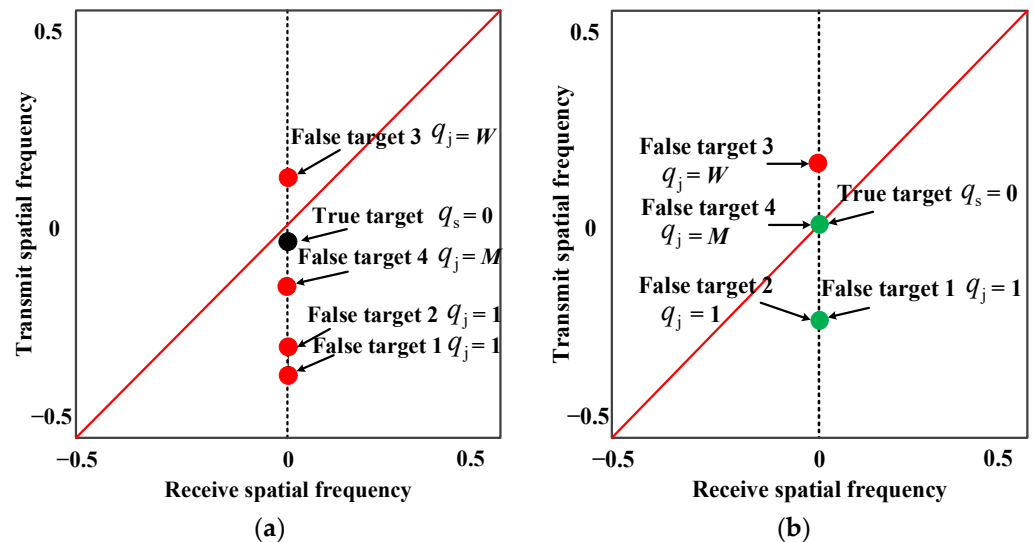
Figure 3. Distribution of the targets in the joint transmit-receive domain. (**a**) Before compensation. (**b**) After compensation.

According to (9) and (16), the difference in the Doppler frequency between the true and the *h*-th targets is

$$\Delta f_d = \Delta f_s - \Delta f_{jh} = q_s\gamma - q_{jh}\gamma = p\gamma \tag{32}$$

where $p = \left| q_s - q_{jh} \right|$ is the delayed pulse difference between the *h*-th false target and the true target. It is observed from (32) that the Doppler frequency difference depends on *p* and γ. By this means, the false targets and the true target can be discriminated in the Doppler frequency domain although they have an identical spatial frequency.

To proceed, a range-angle-Doppler-dependent three-dimensional (3D) beamformer is constructed via the MVDR (Minimum Variance Distortionless Response) criterion, which is written as follows

$$\begin{cases} \min_{w} w^H \widetilde{R} w \\ s.t. w^H \widetilde{u}(\widetilde{R}_s, \theta_0, f_D - \Delta f_s) = 1 \end{cases} \tag{33}$$

where $\widetilde{u}(\widetilde{R}_s, \theta_0, f_D - \Delta f_s) = [b(\theta) \otimes a(\widetilde{R}_s, \theta)] \otimes h^T(f_D - \Delta f_s)$ is the virtual steering vector of the target after compensation, $\widetilde{R}$ is the jammer-plus-noise covariance matrix after compensation, and the optimal weight vector w is calculated as:

$$w = \mu \widetilde{R}^{-1} \widetilde{u}\left(\widetilde{R}_s, \theta, f_D - \Delta f_s\right) \tag{34}$$

where $\mu = \dfrac{1}{\widetilde{u}(\widetilde{R}_s, \theta, f_D - \Delta f_s)^H \widetilde{R}^{-1} \widetilde{u}(\widetilde{R}_s, \theta, f_D - \Delta f_s)}$.

Furthermore, the received data after compensation are processed through the range-angle-Doppler–dependent MVDR beamformer, and the output signal is represented as

$$z = w^H \widetilde{Y} \tag{35}$$

Hence, the false targets are suppressed via range and Doppler mismatches.

3.3. Design of Frequency Increment and Coding Coefficient

In this subsection, the designs of the frequency increment and coding coefficient are investigated. Suppose $q_s = 0$ for simplicity. To begin with, in the transmit frequency domain, the normalized equivalent transmit beampattern for the h-th false target is

$$\begin{aligned} P_T\left(f_T^h\right) &= \frac{1}{M} \frac{\sin\left(\pi M f_T^h\right)}{\sin\left(\pi f_T^h\right)} e^{j2\pi(M-1)(f_T^h)} \\ &= \frac{e^{j\pi(M-1)(-\frac{2\Delta f \widetilde{R}_j}{c} + \frac{d}{\lambda_0}(\sin(\theta) - \sin(\theta_0)))}}{M} \frac{\sin(\pi M Z(p, \theta))}{\sin(\pi Z(p, \theta))} \end{aligned} \tag{36}$$

where $Z(p, \theta) = -\frac{2\Delta f p R_u}{c} + \frac{d}{\lambda_0}(\sin(\theta) - \sin(\theta_0))$, and when the denominator of $P_T\left(f_T^h\right)$ is not zero and the numerator is zero, the nulls of the beampattern exist, i.e.,

$$Z(p, \theta) \begin{cases} = \frac{d}{\lambda_0} \cdot v \frac{\lambda_0}{Md} = v \cdot \frac{1}{M} \\ \neq \frac{d}{\lambda_0} \cdot v \cdot \frac{\lambda_0}{d} = v \end{cases} \tag{37}$$

where $v = 1, 2, \ldots, M - 1$.

Moreover, according to (30) and (31), the difference between the transmit spatial frequencies relative to the true and the h-th false target can be obtained as

$$\Delta f_T = \widetilde{f}_{T,s} - \widetilde{f}_{T,j} = \frac{2\Delta f R_u p}{c} = \frac{\Delta f p}{f_r} = p(b + u) = p(b + \frac{v}{M}), v = 1, \cdots, M - 1 \tag{38}$$

where $b = \text{int}(\frac{\Delta f}{f_r})$ is the integer part and $u = \frac{v}{M}$ is the decimal part. Usually, b can be ignored owing to the 2π periodicity of the exponential term. Notice that the condition $pu \neq 0$ must be satisfied, otherwise, the jammer suppression is invalid because their transmit spatial frequencies are identical. Accordingly, the frequency increment is designed as

$$\Delta f = f_r(b + \frac{v}{M}), v = 1, \cdots, M - 1 \tag{39}$$

Hence, the false targets with $1 \sim M - 1$ delayed pulses are relative to the first to $M - 1$-th nulls of the beampattern, and by nulling at the beampattern, the false targets are suppressed.

Similarly, according to (32), the difference between the false targets and the true target in the Doppler frequency domain can be written as

$$\Delta f_d = p\gamma = p(g + b) \tag{40}$$

where g is the integer part, which is neglected due to the 2π periodicity. b is the fractional part. Similarly, $b \neq 0$ must be guaranteed to distinguish the true and false targets in

the Doppler frequency domain. Assume that $\gamma = \frac{1}{W}$ with W the maximum number of delayed pulses, thus, the false targets which are relative to 1 to $W-1$ delayed pulses can be discriminated and suppressed by satisfying $\Delta f_d = \frac{p}{W} \notin Z^+$.

Figure 4 shows that the targets are distributed in a joint transmit-Doppler domain. It is observed that although the true target and the false target 4 cannot be discriminated in the transmit-receive frequency domain. They are distinguished in the Doppler frequency domain. In contrast, the true target and the false target 3 cannot be discriminated in the Doppler frequency domain because the difference in delayed pulses is W. However, they are distinguished in the transmit-receive frequency domain. Based on the aforementioned observations, by means of nulling in the joint transmit-Doppler frequency domain, the false targets are suppressed. Then, the maximum number of the suppressible false targets in the joint transmit-receive-Doppler domain can be given as

$$D = [M, W] - 1 \tag{41}$$

where $[M, W]$ denotes the least common factor of M and W. To further increase the maximum numbers of the suppressible false targets, M and W are designed to be prime. Hence, the maximum number of suppressible false targets is
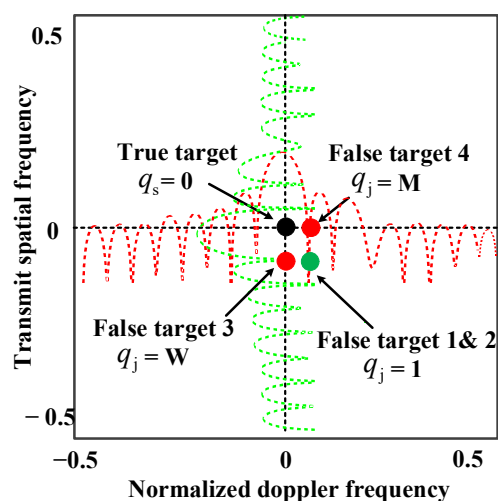
$$D = MW - 1 \tag{42}$$

Figure 4. Distribution of the targets in joint transmit-Doppler domain.

According to (9) and (13), when $f_D > \gamma$, the Doppler frequencies of the targets corresponding to distinct delayed pulses are identical, and the jammer suppression is invalid. Hence, f_d and v_s are no more than $\frac{1}{W}$ of the corresponding maximums, respectively. Accordingly, it is important to choose an appropriate value of W to satisfy the demands of jammers suppression and speed detection simultaneously.

4. Simulations

In this section, simulation results are presented to assess the effectiveness of the jammer suppression method based on the QPC-FDA-MIMO radar. Assume that four false targets are produced in an identical FTG and the delayed pulses for the false targets 1, 2, 3, and 4 are 1, 1, 15 and 16, respectively. The parameters of the QPC-FDA-MIMO system and the targets are, respectively, listed in Tables 1 and 2.

Table 1. Parameters of QPC-FDA-MIMO system.

Parameter	Value	Parameter	Value
The carrier frequency	16 GHz	Pulse repetition frequency	10 kHz
Transmit elements number	16	Receive elements number	16
Transmit elements space	0.0093 m	Receive elements space	0.0093 m
Coding coefficient	1/15	Frequency increment	0.625 kHz

Table 2. Parameters of targets.

	True Target	False Target 1	False Target 2	False Target 3	False Target 4
Angle (°)	0	0	0	0	0
Range(km)	9	20.1	21	232.5	252
Range bin	300	170	200	250	400
Time delay (ms)	0.06	0.134	0.14	1.55	1.68
Velocity (m/s)	10	10	10	10	10
SNR/JNR (dB)	10	20	25	25	25
Delayed pulse	0	1	1	15	16

Figure 5 demonstrates the capon spectrum distributions of the targets in the joint transmit-receive spatial frequency domain. It can be seen from the result that the targets are situated at a straight line with an identical receive spatial frequency in Figure 5a. However, the transmit spatial frequencies depend on the number of delayed pulses and range bins before compensation. In contrast, after range compensation, the same delayed pulse targets are concentrated in an identical transmit spatial frequency. As is intuitively displayed in Figure 5b, false targets 1 and 2 can be discriminated from the true one, while false target 4 cannot be discriminated from the true one because it is located in the same position.
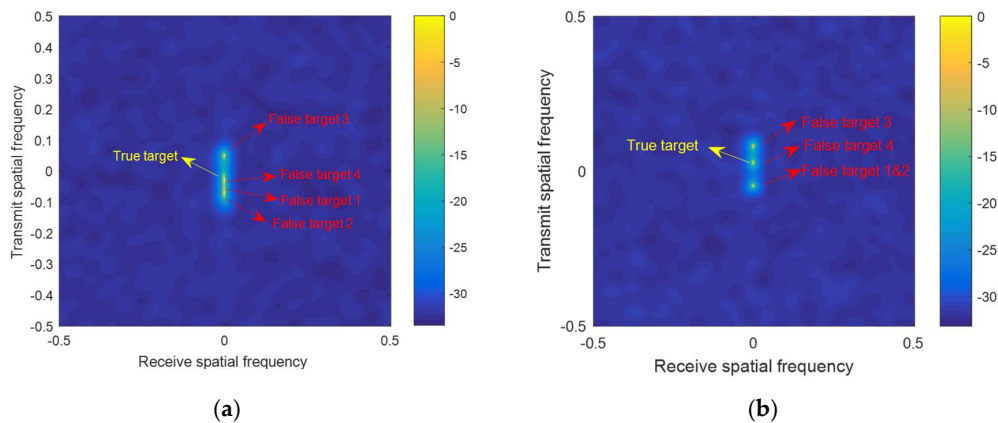

Figure 5. Capon spectrum distributions in the transmit-receive frequency domain. (**a**) Before range compensation. (**b**) After range compensation.

Figure 6 shows the range-Doppler spectrum distributions of the targets. It is observed in Figure 6a that, by projecting onto the Doppler domain, the targets are concentrated with two peaks. In Figure 6b, after demodulation, the true target and the false target 4, which have an identical spatial frequency, are distinguished in the joint range-Doppler frequency domain. However, although the true one and the false target 3 are distinguished in the transmit-receive spatial frequency domain as in Figure 5b, they are not distinguished in the Doppler domain because of the difference in delayed pulses is W. Hence, considering the joint transmit-receive-Doppler domain, all false targets can be discriminated from the true ones.
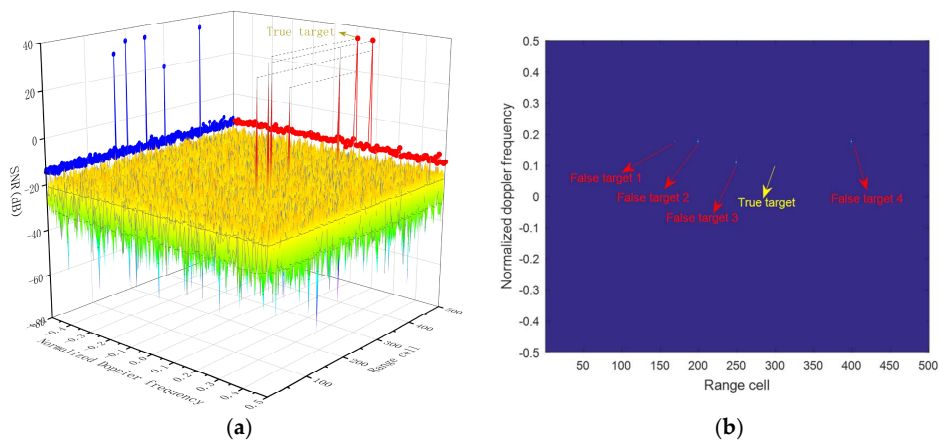
Figure 6. Range-Doppler spectrum distribution. (**a**) 3-D plot. (**b**) 2-D plot.

Figure 7a displays the 3D adaptive beampattern in the joint transmit-receive-Doppler domain. Moreover, the transmit-receive slice of the 3D beampattern is in the QPC-FDA-MIMO radar in Figure 7b, where $f_D - \Delta f_s = 0$. It is observed that the true one is located in the 3-D beampattern's center, and the false target 3, which is suppressed by nulling in the spatial frequency domain, is situated at the same transmit-receive slice with the true one with an identical Doppler frequency in Figure 7b. In addition, the false target 4, which has an identical spatial frequency to the true one, is suppressed by nulling the Doppler domain. Moreover, false targets 1 and 2 can be suppressed by nulling both the Doppler frequency and the spatial frequency domains. On the contrary, the transmit-receive beampattern in the traditional FDA-MIMO radar is plotted in Figure 7c, where distortion of the beampattern occurs because the true target, which has the identical transmit spatial frequency compared with the false target 4.
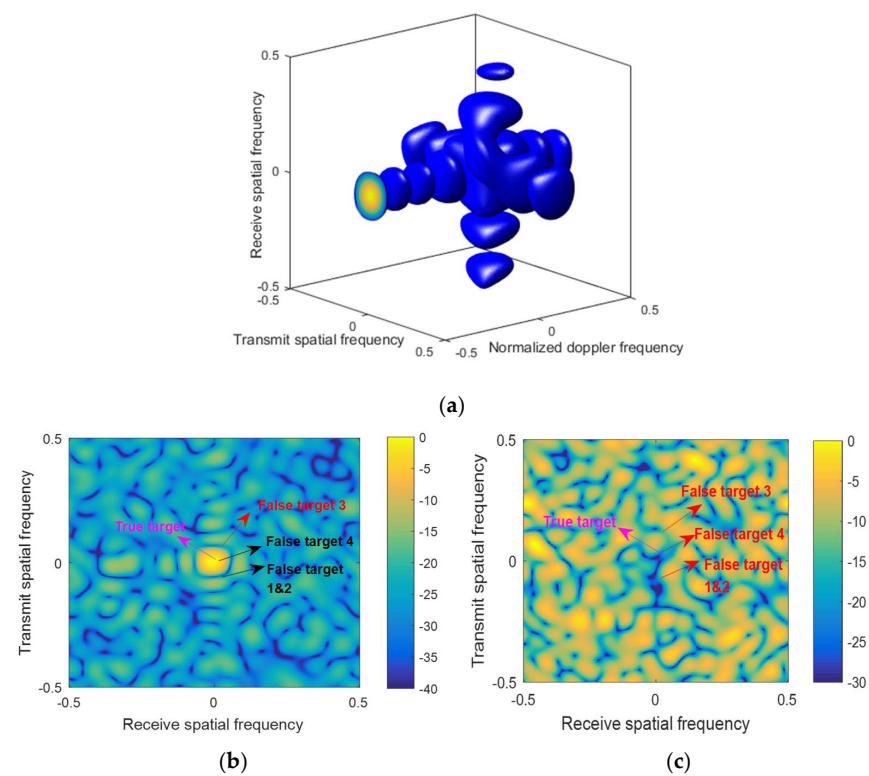

Figure 7. Beampatterns. (**a**) Transmit-receive-Doppler 3D beampattern of the QPC-FDA-MIMO radar. (**b**) Transmit-receive slice of the 3D beampattern of the QPC-FDA-MIMO radar. (**c**) Transmit-receive beampattern of the FDA-MIMO radar.

Furthermore, as is shown in Figure 8 that comparisons of the output powers among distinct radar frameworks are also provided. The true target has the maximum output power in the QPC-FDA-MIMO radar, where the false targets are suppressed in the joint transmit-receive-Doppler domain. In contrast, the false targets, whose delayed pulses are more than $M - 1$ (such as false target 4), cannot be suppressed in the EPC-MIMO radar and FDA-MIMO radar.
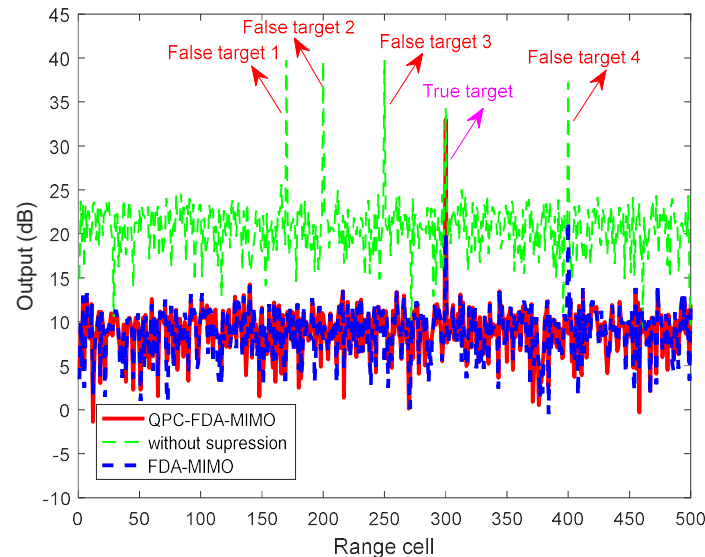
Figure 8. Comparison of output results.

The zones of false target suppression are shown in Figure 9, where the y-axis and the x-axis denote the coding coefficient and the number of delayed pulses, respectively. Particularly, the yellow color indicates effective suppression, and the blue color indicates that the jammer's suppression is invalid. As is intuitively shown in Figure 9a,b, by modulating with the same phase in both EPC-MIMO and FDA-MIMO, the first to the $M - 1$-th nulls of the beampattern correspond to the false targets; the first to the $M - 1$-th delayed pulses and the maximum number of suppressible jammers is $M - 1$. It is worth pointing out that, by setting $\gamma = 1/W$ and $W = M - 1$, the maximum number of suppressible jammers is $(M - 1)(M - 2)$. Hence, the proposed method has superiorities in improving the maximum number of suppressible jammers, which is in agreement with the theoretical analyses.

Figure 10 shows the output signal-to-jammer-plus-noise ratio (SJNR) curves versus input signal-to-noise ratio (SNR) among different radar frameworks with 150 Monte Carlo (MC) trails. What is more, the upper bound is provided as an ideal case. Remarkably, both the EPC-MIMO and FDA-MIMO radars cannot suppress the false target whose delayed pulse number is M, i.e., the false target 4, leading to a low SJNR. In contrast, all false targets are effectively suppressed by means of utilizing the data-dependent transmit-receive-Doppler 3D beamforming in QPC-FDA-MIMO which improves the output SJNR performance.
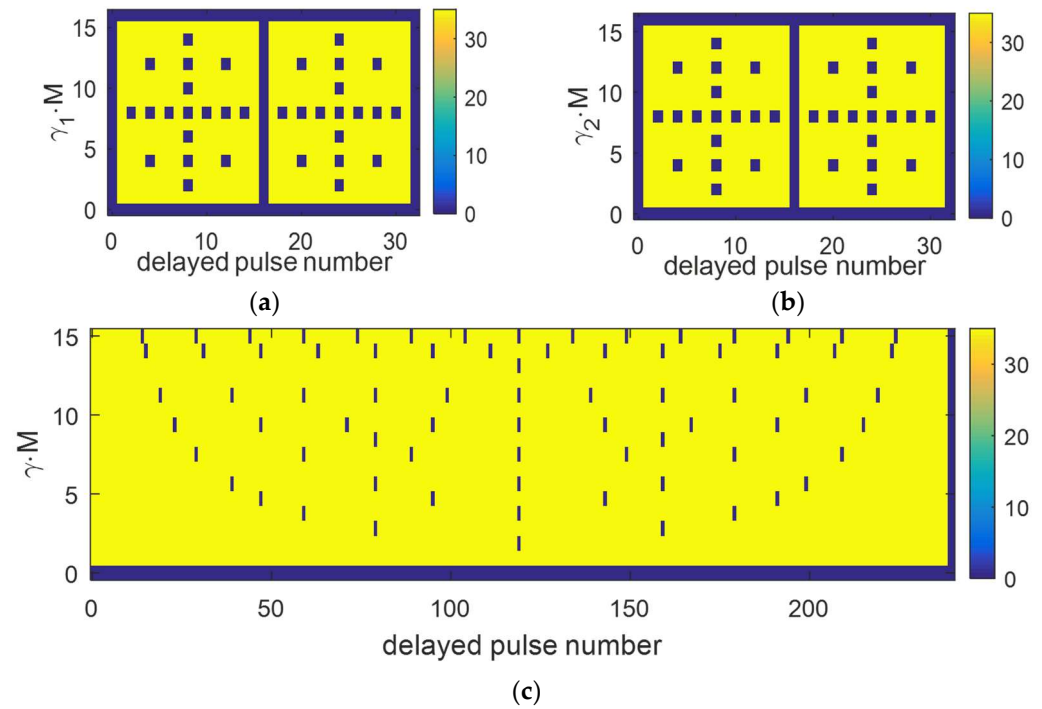
Figure 9. Suppression zones of false targets. (**a**) EPC-MIMO. (**b**) FDA-MIMO. (**c**) QPC-FDA-MIMO.
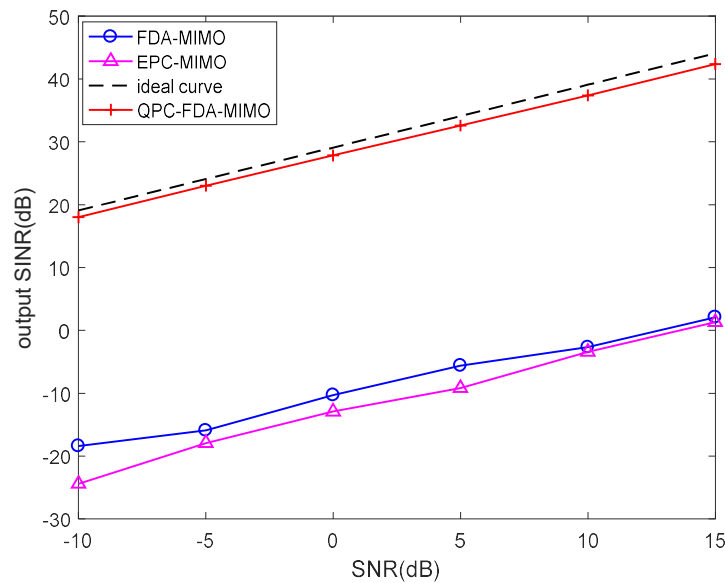

Figure 10. Output SJNR performance with respect to input SNR.

5. Conclusions

In this paper, the method to suppress the main lobe deceptive jammers has been presented in the QPC-FDA-MIMO radar. In the modeling phase, QPC has been applied along the slow time dimension in the transmit array of the FDA-MIMO radar. At the receiver, the decoding and principal range compensation has been carried out to distinguish the false targets and the true target in the transmit-receive-Doppler frequency domain. Then, by performing the data-dependent transmit-receive-Doppler 3D beamforming, the false targets have been suppressed. Moreover, the coding coefficient and frequency increments have been designed to increase the maximum number of suppressible jammers. Numerical results have been presented to assess the jammer suppression performance, where comparisons among various frameworks, containing FDA-MIMO and EPC-MIMO radars, have been carried out in terms of the spectrum distribution and output SJNR. The suppression

performance has been ensured and the maximum number of suppressible jammers is obviously improved in the QPC-FDA-MIMO radar.

In the future, the suppression of fast-generated false targets delayed in the same transmit pulse in comparison with the true target will be concentrated on and the scenario of multiple true targets will be considered.

References

1. Jin, F.; Cao, S. Automotive Radar Interference Mitigation Using Adaptive Noise Canceller. *IEEE Trans. Veh. Technol.* **2019**, *68*, 3747–3754. [CrossRef]
2. Neemat, S.; Krasnov, O.; Yarovoy, A. An interference mitigation technique for FMCW radar using beat-frequencies interpo-lation in the STFT domain. *IEEE Trans. Microw. Theory Tech.* **2019**, *67*, 1207–1220. [CrossRef]
3. Wen, W.; So, H. Transmit Subaperturing for Range and Angle Estimation in Frequency Diverse Array Radar. *IEEE Trans. Signal Process.* **2014**, *62*, 2000–2011.
4. Cui, G.; Fu, Y.; Yu, X.; Li, J. Robust Transmitter–Receiver Design in the Presence of Signal-Dependent Clutter. *IEEE Trans. Aerosp. Electron. Syst.* **2018**, *54*, 1871–1882. [CrossRef]
5. Wen, W.; Hing, S.; Alfonso, F. FDA-MIMO Signal Processing for Mainlobe Jammer Suppression. In Proceedings of the 2019 27th European Signal Processing Conference (EUSIPCO), A Coruna, Spain, 2–6 September 2019; pp. 1–5.
6. Jung, H.; Van Nguyen, B.; Song, I.; Kim, K. Design of Anti-Jamming Waveforms for Time-Hopping Spread Spectrum Systems in Tone Jamming Environments. *IEEE Trans. Veh. Technol.* **2020**, *69*, 728–737. [CrossRef]
7. Yu, X.; Cui, G.; Yang, J.; Kong, L. MIMO Radar Transmit–Receive Design for Moving Target Detection in Signal-Dependent Clutter. *IEEE Trans. Veh. Technol.* **2020**, *69*, 522–536. [CrossRef]
8. Al-Salehi, A.R.; Qureshi, I.M.; Malik, A.N.; Khan, Z.; Khan, W. Throughput Enhancement for Dual-Function Radar-Embedded Communications Using Two Generalized Sidelobe Cancellers. *IEEE Access* **2019**, *7*, 91390–91398. [CrossRef]
9. Li, Z.; Ye, H.; Liu, Z.; Sun, Z.; An, H.; Wu, J.; Yang, J. Bistatic SAR Clutter-Ridge Matched STAP Method for Nonstationary Clutter Suppression. *IEEE Trans. Geosci. Remote Sens.* **2021**, *60*, 1–14. [CrossRef]
10. Chang, S.; Deng, Y.; Zhang, Y.; Zhao, Q.; Wang, R.; Zhang, K. An Advanced Scheme for Range Ambiguity Suppression of Spaceborne SAR Based on Blind Source Separation. *IEEE Trans. Geosci. Remote Sens.* **2022**, *60*, 1–12. [CrossRef]
11. Al-Tous, H.; Barhumi, I.; Al-Dhahir, N. Narrow-Band Interference Mitigation Using Compressive Sensing for AF-OFDM Systems. *IEEE Trans. Veh. Technol.* **2017**, *66*, 6146–6159. [CrossRef]
12. Yang, J.; Thompson, J.; Huang, X.; Jin, T.; Zhou, Z. Random-Frequency SAR Imaging Based on Compressed Sensing. *IEEE Trans. Geosci. Remote Sens.* **2013**, *51*, 983–994. [CrossRef]
13. Lin, Z.; Chen, Y.; Liu, X.; Jiang, R.; Shen, B. Adaptive Beamforming Design of Planar Arrays Based on Bayesian Compressive Sensing. *IEEE Sensors J.* **2021**, *21*, 5185–5194. [CrossRef]
14. Yang, J.; Jin, T.; Huang, X.; Thompson, J.; Zhou, Z. Sparse MIMO Array Forward-Looking GPR Imaging Based on Compressed Sensing in Clutter Environment. *IEEE Trans. Geosci. Remote Sens.* **2014**, *52*, 4480–4494. [CrossRef]
15. Zhang, X.; Ma, H.; Wang, J.; Zhou, S.; Liu, H. Game Theory Design for Deceptive Jamming Suppression in Polarization MIMO Radar. *IEEE Access* **2019**, *7*, 114191–114202. [CrossRef]
16. Jabran, A.; Karl, E. Frequency Agility Radar with Overlapping Pulses and Sparse Reconstruction. In Proceedings of the 2018 IEEE Radar Conference (RadarConf18), Oklahoma City, OK, USA, 23–27 April 2018; pp. 0061–0066.
17. Tang, Z.; Deng, Y.; Zheng, H.; Wang, R. High-Fidelity SAR Intermittent Sampling Deceptive Jamming Suppression Using Azimuth Phase Coding. *IEEE Geosci. Remote Sens. Lett.* **2021**, *18*, 489–493. [CrossRef]
18. Amin, M.; Zhao, L.; Lindsey, A. Subspace array processing for the suppression of FM jamming in GPS receivers. *IEEE Trans. Aerosp. Electron. Syst.* **2004**, *40*, 80–92. [CrossRef]
19. Yang, X.; Zhang, Z.; Zeng, T.; Long, T.; Sarkar, T.K. Mainlobe Interference Suppression Based on Eigen-Projection Processing and Covariance Matrix Reconstruction. *IEEE Antennas Wirel. Propag. Lett.* **2014**, *13*, 1369–1372. [CrossRef]

20. Chen, H.-F.; Cao, X.-R.; Fang, H.-T.; Zhu, J. Nonlinear adaptive blind whitening for MIMO channels. *IEEE Trans. Signal Process.* **2005**, *53*, 2635–2647. [CrossRef]

21. Ting, S.; Yong, G. TDOA estimation of dual-satellites interference localization based on blind separation. *J. Syst. Eng. Electron.* **2019**, *30*, 696–702.

22. Ge, M.; Cui, G.; Kong, L. Main lobe jamming suppression for distributed radar via joint blind source separation. *IET Radar Sonar Navig.* **2019**, *13*, 1189–1199. [CrossRef]

23. Ma, J.; Shi, L.; Xiao, S.; Wang, X. Mitigation of cross-eye jamming using a dual-polarization array. *J. Syst. Eng. Electron.* **2018**, *29*, 491–498.

24. Park, K.; Seo, J. Single-antenna-based GPS anti-jamming method exploiting polarization diversity. *IEEE Trans. Aer-Ospace Electron. Syst.* **2021**, *57*, 919–934. [CrossRef]

25. Dai, H.; Wang, X.; Li, Y.; Liu, Y.; Xiao, S. Main-Lobe Jamming Suppression Method of using Spatial Polarization Characteristics of Antennas. *IEEE Trans. Aerosp. Electron. Syst.* **2012**, *48*, 2167–2179. [CrossRef]

26. Xu, J.; Liao, G.; Zhu, S.; Huang, L.; So, H.C. Joint Range and Angle Estimation Using MIMO Radar With Frequency Diverse Array. *IEEE Trans. Signal Process.* **2015**, *63*, 3396–3410. [CrossRef]

27. Sammartino, P.; Baker, C.; Griffiths, H. Frequency diverse MIMO techniques for radar. *IEEE Trans. Aerosp. Electron. Syst.* **2013**, *49*, 201–222. [CrossRef]

28. Lan, L.; Marino, A.; Aubry, A.; De Maio, A.; Liao, G.; Xu, J.; Zhang, Y. GLRT-Based Adaptive Target Detection in FDA-MIMO Radar. *IEEE Trans. Aerosp. Electron. Syst.* **2021**, *57*, 597–613. [CrossRef]

29. Xu, J.; Zhu, S.; Liao, G. Range Ambiguous Clutter Suppression for Airborne FDA-STAP Radar. *IEEE J. Sel. Top. Signal Process.* **2015**, *9*, 1620–1631. [CrossRef]

30. Lan, L.; Xu, J.; Liao, G.; Zhang, Y.; Fioranelli, F.; So, H.C. Suppression of Mainbeam Deceptive Jammer With FDA-MIMO Radar. *IEEE Trans. Veh. Technol.* **2020**, *69*, 11584–11598. [CrossRef]

31. Xu, J.; Liao, G.; Zhang, Y.; Ji, H.; Huang, L. An Adaptive Range-Angle-Doppler Processing Approach for FDA-MIMO Radar Using Three-Dimensional Localization. *IEEE J. Sel. Top. Signal Process.* **2016**, *11*, 309–320. [CrossRef]

32. Lan, L.; Liao, G.; Xu, J.; Zhang, Y.; Fioranelli, F. Suppression approach to main-beam deceptive jamming in FDA-MIMO radar using nonhomo-geneous sample detection. *IEEE Access* **2018**, *6*, 34582–34597. [CrossRef]

33. Wang, W.-Q.; So, H.C.; Farina, A. An Overview on Time/Frequency Modulated Array Processing. *IEEE J. Sel. Top. Signal Process.* **2017**, *11*, 228–246. [CrossRef]

34. Xu, J.; Liao, G.; Zhu, S.; So, H.C. Deceptive jamming suppression with frequency diverse MIMO radar. *Signal Process.* **2015**, *113*, 9–17. [CrossRef]

35. Lan, L.; Liao, G.; Xu, J.; Zhang, Y.; Liao, B. Transceive Beamforming With Accurate Nulling in FDA-MIMO Radar for Imaging. *IEEE Trans. Geosci. Remote Sens.* **2020**, *58*, 4145–4159. [CrossRef]

36. Xu, J.; Zhang, Y.; Liao, G.; So, H.C. Resolving Range Ambiguity via Multiple-Input Multiple-Output Radar With Element-Pulse Coding. *IEEE Trans. Signal Process.* **2020**, *68*, 2770–2783. [CrossRef]

37. Lan, L.; Liao, G.; Xu, J.; Zhang, Y.; Zhu, S. Mainlobe deceptive jammer suppression using element-pulse coding with MIMO radar. *Signal Process.* **2021**, *182*, 107955. [CrossRef]

38. Zhang, X.; Cao, D.; Xu, L. Joint polarisation and frequency diversity for deceptive jamming suppression in MIMO radar. *IET Radar Sonar Navig.* **2019**, *13*, 263–271. [CrossRef]

39. Liu, Q.; Xu, J.; Ding, Z.; So, H.C. Target Localization With Jammer Removal Using Frequency Diverse Array. *IEEE Trans. Veh. Technol.* **2020**, *69*, 11685–11696. [CrossRef]

40. Ge, J.; Xie, J.; Wang, B. A cognitive active anti-jamming method based on frequency diverse array radar phase center. *Digit. Signal Process.* **2021**, *109*, 102915. [CrossRef]